Infrared grey-field polariscope: A tool for rapid stress analysis in microelectronic materials and devices

Gavin Horn[a)]
The University of Illinois at Urbana-Champaign, 1206 West Green Street, Urbana, Illinois 61802

Jon Lesniak
Stress Photonics, Inc., 3002 Progress Road, Madison, Wisconsin 53716

Thomas Mackin
The University of Illinois at Urbana-Champaign, 1206 West Green Street, Urbana, Illinois 61802

Brad Boyce
Stress Photonics, Inc., 3002 Progress Road, Madison, Wisconsin 53716

The infrared grey-field polariscope (IR-GFP) has been developed to provide rapid, full-field stress analysis for infrared-transparent materials. Grey-field photoelastic theory is outlined and the advantages of this implementation for microelectronic materials inspection highlighted. The capabilities of this scientific tool are proven using standard sample geometries fabricated from single crystal silicon substrates and the general applicability of the instrument demonstrated on bonded devices and silicon wafer geometries. Stress resolution in silicon wafers is better than 0.1 MPa at wafer inspection speeds of 10 s for a 100 mm wafer. Initial applications of the IR-GFP have shown that the tool provides improvements in defect detection and stress quantification when compared to conventional infrared transmission imaging while also providing several important advantages over other currently utilized inspection technologies. © *2005 American Institute of Physics.* [DOI: 10.1063/1.1884189]

I. INTRODUCTION

Semiconductor fabrication continues to move toward larger wafers, thinner films, and smaller packages, a trend that places growing demands on process control. Of particular interest is the role of allowable residual stresses that arise from thermal mismatch, material mismatch, or contamination during wafer bonding. Failures arising from thermal and residual stresses play a key role in manufacturability, suggesting that a more detailed understanding of the stress within, and between, materials could significantly improve manufacturability and reliability. Online inspection during manufacturing could significantly improve yields, especially if that inspection was used to inform and improve the manufacturing process.

Several stress analysis techniques have been developed for silicon substrate and device inspection. The most common techniques measure changes in elastic properties (e.g., x-ray diffraction, acoustic microscopy) or stress-induced curvature of a device or structure (e.g., reflected laser, interferometry, coherent gradient sensing). x-ray diffraction offers the highest sensitivity and is widely used in both industry and academia. This nondestructive, single-point technique measures changes in the crystal lattice spacing to determine residual stresses.[1] Incredibly high strain sensitivities on the order of 10^{-8} can be obtained for large Bragg angles and

sensitivity on the order of $10^{-5} - 10^{-4}$ is possible for angles of approximately 45°. Though highly sensitive, the small spot sizes and long inspection times render x-ray diffraction unsuited to real-time inspection in an industrial setting.

Scanning acoustic microscopy is a full-field, nondestructive technique capable of detecting changes in elastic properties of solids.[2] Compared to x-ray topography, this technique is relatively quick and inexpensive, and is applicable to both crystalline and amorphous materials. An important drawback of acoustic microscopy is that measurements must be carried out in a coupling liquid and the sample must be rastered in order to present two-dimensional images, again rendering this technique unsuitable to real-time, on-line inspections.

Laser scanning is commonly used to infer residual stresses in thin films by measuring changes in substrate curvature. This nondestructive optical technique sweeps a laser beam across the substrate to generate a map of reflection angles that are converted into sample curvatures.[3,4] The global curvature is then used to calculate the elastic stress distribution usually utilizing Stoney's formula.[5] To do so one needs to know precisely the thickness and elastic properties of the substrate and film layers. The laser scanning technique can measure radius of curvatures up to 10^4 m and is often implemented as an *in situ* measurement during thin film deposition. However, because this method provides global average information, local variations in the stress state will be missed. When measuring stresses caused by thin film growth, it is often necessary to scan the wafer before and

_____

[a)]Author to whom correspondence should be addressed; electronic mail: ghorn@uiuc.edu

after the thin film has been grown or deposited, and use a differential method to obtain reliable results.

An important alternative to laser scanning, named the multi-beam optical stress sensor (MOSS),[6] employs a highly reflective etalon to convert a single laser beam into five parallel beams, spaced at controlled intervals, that measures curvatures as large as 4 km.[7] The MOSS is nondestructive, noncontacting, is applicable to real-time inspection and does not require vibration isolation. The apparatus is limited to five beams due to reflective losses in the etalon, so spatial averaging occurs over the distance between the beams, resulting in loss of resolution in thicker wafers. Again, this is a continuum approach that assumes *a priori* knowledge of the film thickness and properties.

Optical interferometric techniques are generally real-time, full field and noncontacting means for curvature measurements. Several methods are available, but Moiré is most commonly applied to electronic packaging,[8] while a grazing incidence Moiré technique[9] and a Twyman–Green interferometer[10] have been reported for measuring curvature after film deposition. These techniques benefit from being very rapid and noncontacting and can be used *in situ*. However, in many cases packages must be sectioned and the need for a specimen grating will often damage or destroy the samples being inspected. These techniques are also sensitive to rigid body displacements and rotations and must be vibration isolated in order to produce reliable results.

The coherent gradient sensing (CGS) method was developed by Tippur, Krishnaswamy, Rosakis in 1990 for mapping crack tip deformations[11] and was applied as a tool for measuring curvature in thin film systems in 1998.[12] CGS is a full-field, real-time, nonintrusive, and noncontacting technique that measures curvature tensor fields. This technique measures gradients of displacement rather than actual displacements, which means that it is not sensitive to rigid body rotations or translations and does not need to be vibration isolated.

A technique that has shown promise for providing very sensitive residual stress measurement is infrared photoelastic stress analysis. The method is based upon the well-established principles of photoelasticity, wherein stresses are known to change the speed of light in photoelastic materials. In this article, we introduce the recently developed infrared grey-field polariscope (IR-GFP) as a full-field optical technique for high-resolution, rapid measurement of stresses in silicon devices. This method is demonstrated using several canonical geometries and extension to defect location applications in semiconductors is outlined.

II. OVERVIEW OF INFRARED PHOTOELASTICITY

In 1816, Sir David Brewster discovered that the natural double refractive indices seen in many transparent materials can be varied artificially in proportion to applied stress,[13] a phenomenon that became known as the photoelastic effect. Lacking technology to further the discovery, significant advances were not made until the early 20th century.[14] All of the pioneering works in photoelasticity were completed using visible light; however, nothing in the electromagnetic-field equations limits stress-induced birefringence to the visible portion of the spectrum. In the mid-1950's, Dash found proof of birefringence in silicon using infrared light.[15] A few years later, Appel and Pontarelli introduced what is believed to be the first infrared polariscope.[16] Shortly thereafter, Lederhandler published the first images of residual stresses in silicon wafers measured using an infrared polariscope.[17] Throughout the 60's, 70's, and early 80's interest increased as investigators built polariscopes using both plane and circularly polarized light[18–20] and began investigating a wider range of materials.[21–23]

Since the late 80's, Yamada has dominated the field of research with infrared photoelasticity.[24] In 1993 he unveiled his first computer controlled infrared polariscope.[25] Yamada's group has shown that residual stresses in GaAs wafers depend on where the slice was removed from an ingot,[26] that residual stresses strongly depend on the growth method,[27,28] that residual stresses are relieved by cracking[29] and that wafer mounting geometry plays an important role in the residual stress evolution during annealing.[30,31] For InP wafers, they have compared growth[32,33] and annealing techniques.[34] Recently, Fukuzawa and Yamada have suggested that their scanning infrared polariscope would be useful for silicon wafer inspection and process evaluation.[35] The main drawback of this system is that it uses a single-point scanning detector. As such, each wafer must be mounted on a translating stage and scanned, point by point, to generate a full-field wafer image. Inspection speed has improved with recent technological advances, but has not overcome the inherent limiations of a single-point detector. As a result of their vast experience, Yamada's group has shown that the infrared photoelastic *technique* can provide very sensitive stress analysis in semiconductor materials. The widespread adoption of the method, however, has been limited by their single-point scanning approach.

In the 90's Niitsu developed a polariscope that employs a high frequency photoelastic modulator which converts linearly polarized light into oscillating elliptical light.[36,37] As with Yamada's system, Niitsu utilizes a single photodetector to scan across the wafer, resulting in long scan times for a single wafer. Resolution is also limited by the round laser spot, which measures slightly less than 1 mm.[38] Since the early 90's, Zhao's group has been using an infrared polariscope that implements more classical techniques.[39] They employ a simple plane and circular polariscope and manually count fringes to obtain a measure of stress. All of their investigations have imaged silicon from the edge so that their optical path length is very long, allowing the detection of small retardations.[40,41]

More recently, Zheng and Danyluk[42,43] implemented a full-field phase stepping technique and employ a fringe multiplication method, which increased their stress resolution, but also reduced their spatial resolution. An equally valuable contribution of their work is that the angular dependence of the stress-optic coefficient and deviation angle of the principal orientations of in-plane refractive indices for a (100) wafer of silicon were determined in closed form. When a (100) silicon wafer is inspected in the [001] direction using 1.15 μm near-infrared light, the relative stress-optic coeffi-

cient can be related to the angle (θ) between the principle stress orientation and the [110] directions by[43]

$$C_{(100)} = (2.657 \sin^2 2\theta + 0.707 \cos^2 2\theta)^* 10^{-11} \text{ Pa}^{-1}. \quad (1)$$

A recent system has been introduced[44] using a single-point laser scanning technique based on similar principles to those developed by Yamada. This scanning infrared depolarization measurement method utilizes a single 1.3 μm wavelength linearly polarized laser beam of 100 μm spot size to illuminate silicon wafers, with a beam splitter and two photodiodes behind orthogonal polarizers to detect the transmitted light. To improve sensitivity, they implement a homodyne detection scheme. They report inspection times of about 5 min for an entire 300 mm wafer,[44] which is remarkably faster than the Yamada system. The published applications for this tool are focused on stress and defect observation in the wafer manufacturing industry,[44,45] locating small defects by imaging the large stress region. This method displays good stress sensitivity, but is again limited by using a scanning implementation and limitations of the laser source. Rough surfaces will cause significant scattering and depolarization of the laser. Very rough surfaces may knock out so much light that this technique is not viable. Spatial resolution and minimum scanning times are fixed by the laser spot size. Furthermore, the linearly polarized source will cause superposition of retardation due to residual stress magnitude and direction, which may limit the ability to collect quantifiable data.

III. PRINCIPLE OF GREY-FIELD PHOTOELASTICITY

The visible light grey-field polariscope (GFP) was originally developed with NASA[46] to provide high-resolution, full-field, subfringe photoelastic stress analysis in materials transparent to visible light.[47] The following section provides a short primer on the basics of photoelasticity as well as a brief description of grey-field photoelastic technology condensed from the previous references

The grey-field polariscope is a fusion of a circular polariscope with a plane polariscope. The GFP illuminates the object with circularly polarized light, yet analyzes the transmitted light using a simple rotating linear analyzer. Figure 1 shows a schematic representation of the apparatus inspecting a strained coating in reflection mode. Circularly polarized light is simply two orthogonal linear polarized light vectors that are 1/4 period (90°) out of phase. Considering only the vector sum of these two waves, circularly polarized light is described as a single light vector of constant amplitude that rotates about the axes on which it propagates. By viewing these waves along the propagation axes, the head of the resultant light vector sweeps out a circle.

After propagating through a stressed stress-birefringent material, the portion of circular light along the slow axis is retarded by a phase lag, Δ, with respect to light propagating along the fast axis of the sample is given by
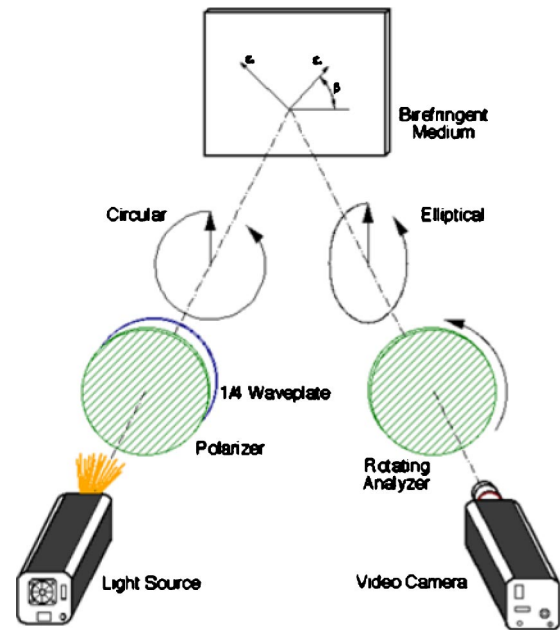

FIG. 1. (Color online). Grey-field reflection polariscope (see Ref. 46).

$$\Delta = \frac{2\pi C d}{\lambda}(\sigma_1 - \sigma_2), \quad (2)$$

where d is the material thickness, λ is the wavelength of light, C is the stress optic coefficient of the material, and σ_1 and σ_2 are the first and second principal stresses.

The two orthogonal light components of the transmitted light are no longer 90° out of phase so that light exiting the material now takes an elliptical shape with fast and slow axis transmission amplitudes given by

$$A_1' = a \cos\left(\omega t + \frac{\Delta}{2} + \beta\right), \quad (3a)$$

$$A_2' = -a \sin\left(\omega t - \frac{\Delta}{2} + \beta\right), \quad (3b)$$

where a is the amplitude of the circularly polarized light and ω is the temporal angular frequency of the wave. This equation can be rewritten to express the amplitude of the resulting elliptical light, along the major and minor axes, as

$$A_{\text{maj}} = \sqrt{2}a \cos\left(\frac{\pi}{4} - \frac{\Delta}{2}\right)\cos\left(\omega t + \frac{\pi}{4} + \beta\right), \quad (4a)$$

$$A_{\text{min}} = \sqrt{2}a \cos\left(\frac{\pi}{4} + \frac{\Delta}{2}\right)\sin\left(\omega t + \frac{\pi}{4} + \beta\right). \quad (4b)$$

In these equations, β is the orientation of the fast axis. As the second term in Eq. (4a) shows, the major axis of the ellipse is generally shifted $\pi/4$ radians from the direction of the first principal strain for $\Delta < \pi/2$. This shift is material dependent, but for silicon the relationship is available in the literature.[43] Determination of the principal stress direction is an additional piece of information gleaned by projecting circularly polarized light as opposed to linear. The key point is that the geometry of elliptical light mirrors the magnitude of the difference in the first and second principal stresses as well as the orientation of the principal stresses.

In grey-field photoelasticity, a rotating analyzer is placed in front of the detector unit to selectively pass only that light orientated along its transmission axis. As the analyzer rotates, the intensity of transmitted light is a maximum when the polarizer aligns with the major axis and a minimum when the polarizer aligns with the minor axis of the ellipse, with trigonometric transitions in between. For a given analyzer orientation α, the sum of the projections of the major and minor components of light is given by

$$A_\alpha = A_{\text{maj}} \cos\left(\alpha - \frac{\pi}{4} - \beta\right) + A_{\text{min}} \sin\left(\alpha - \frac{\pi}{4} - \beta\right). \quad (5)$$

The intensity of the transmitted light (square of the amplitude) is dependent on the angular position of the rotating polarizer, α, which is given by

$$I = a^2[1 + \sin 2(\alpha - \beta)\sin \Delta]. \quad (6)$$

If no stress is present in the birefringent material, $\sin \Delta$ is zero, and the transmitted light is circularly polarized. However, in the presence of shear stress in a birefringent material, $\sin \Delta$ has a finite value. As the analyzer transmission axis will align with the major axis twice per full rotation, the intensity will be modulated at 2α with phase of 2β.

Restating Eq. (6) in terms of this modulation frequency ($\sin 2\alpha$ and $\cos 2\alpha$), the intensity measured by the detector unit is given by

$$I = I_a + I_{c\alpha} \cos 2\alpha + I_{s\alpha} \sin 2\alpha, \quad (7)$$

where

$$I_{c\alpha} = -(a^2 \sin \Delta)\sin 2\beta, \quad (8a)$$

$$I_{s\alpha} = (a^2 \sin \Delta)\cos 2\beta \quad (8b)$$

and I_a is the average light intensity collected by the detector unit. Due to less than ideal experimental conditions, the average light term often has components from polarized, scattered, and incident ambient light. It is convenient to normalize the measured signal, I, by the time averaged light intensity I_a, eliminating the effects of spurious illumination as follows:

$$\bar{I} = 1 + \bar{I}_{c\alpha} \cos 2\alpha + \bar{I}_{s\alpha} \sin 2\alpha, \quad (9)$$

where

$$\bar{I}_{c\alpha} = -(\eta \sin \Delta)\sin 2\beta, \quad \text{and} \quad \bar{I}_{s\alpha} = (\eta \sin \Delta)\cos 2\beta \quad (10)$$

and η is the polarization intensity. The normalized intensity is only a function of the known polarizer position and polarization intensity and the desired quantities: phase retardation (i.e., shear stress magnitude), and the principal stress direction.

Rearranging Eqs. (10), the retardation and direction of the first principal strains are related to the $I_{c\alpha}$ and $I_{s\alpha}$ by

$$\sin \Delta = \frac{1}{\eta}(\bar{I}_{c\alpha}^2 + \bar{I}_{s\alpha}^2)^{1/2}, \quad (11)$$

$$\beta = \frac{1}{2} \tan^{-1}\left(-\frac{\bar{I}_{c\alpha}}{\bar{I}_{s\alpha}}\right). \quad (12)$$
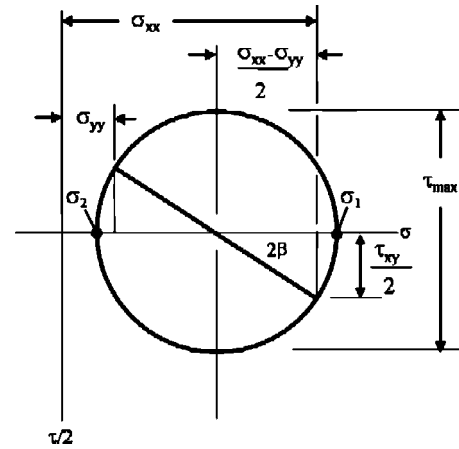

FIG. 2. Mohr's circle for stress.

For many applications of interest (especially in the microelectronics industry), the instrument must detect very small shear strains in very thin test samples. From Eq. (2) it is apparent that these conditions may well give rise to very small optical retardations. In these cases, the amplitude of the phase retardation is directly related to the magnitude of the shear strains. For very small retardation angles the trigonometric relationship can be simplified by $\sin \Delta \approx \Delta$, and Eq. (11) rewritten as

$$\Delta = \frac{1}{\eta}(\bar{I}_{c\alpha}^2 + \bar{I}_{s\alpha}^2)^{1/2}. \quad (13)$$

This type of analysis is typically termed subfringe photoelasticity, since the retardations are not sufficient to generate a series of distinct intensity bands.

In order to measure the elliptical light intensities, an analog encoder is attached to the rotating analyzer to directly determine the polarizer position, α. In the current generation of instrument 16 images of the transmitted light are collected over one complete rotation of the analyzer. By knowing the analyzer position and using a simple video algorithm, these 16 images are correlated with reference functions representing the three intensity components of Eq. (7). The normalizing procedure of Eq. (9) is then performed. Finally, the quantities of interest, Δ and β, are determined from Eqs. (13) and (12), and the magnitude of the shear stress calculated using Eq. (2).

The sine and cosine components $(\bar{I}_{s\alpha}, \bar{I}_{c\alpha})$ of the light intensity are directly related to the stresses along the 0/90° and ±45° planes. To understand this concept, we begin with Mohr's circle, the radius of which is $(\sigma_1 - \sigma_2)/2$. By inspection of Eq. (2), this value is directly related to Δ, and from, Eq. (13), is directly related to the magnitude of the light intensity recorded by the detector. From the geometry shown in Fig. 2, the cosine component of Mohr's circle radius is $(\sigma_{xx} - \sigma_{yy})/2$ and the sine component is $\tau_{xy}/2$ or equivalently $(\sigma_{+45} - \sigma_{-45})/2$. Equations (10) show that the cosine component of total intensity amplitude is given by $\bar{I}_{s\alpha}$ and the sine component given by $\bar{I}_{c\alpha}$. Thus, for subfringe measurements

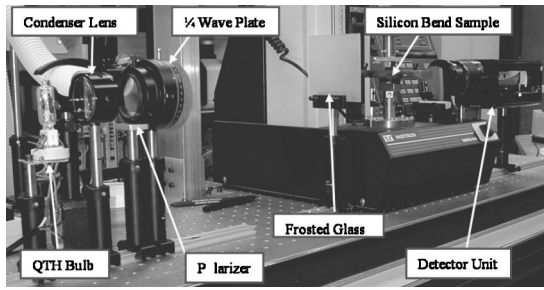$$\bar{I}_{s\alpha} \propto (\sigma_{xx} - \sigma_{yy}) \quad \text{and} \quad (14a)$$

FIG. 3. Prototype IR-GFP system fixtured for a four point bend sample.

FIG. 4. Four-point bend sample.

$$\bar{I}_{c\alpha} \propto \tau_{xy} \ or \ (\sigma_{+45} - \sigma_{-45}). \tag{14b}$$

As a result of this analysis, GFP data are reported as the difference in principle stresses in the 0/90 and ±45 orientations. In the following experiments, light will be transmitted along the [001] direction of the (100) silicon orientation, and the $\bar{I}_{s\alpha}, \bar{I}_{c\alpha}$ components will measure differences in stresses in the [100] and [110] directions, respectively.

In traditional photoelastic analysis, total optical retardation is related to the principal stress difference, but the orientation of the principal stresses may not be known *a priori*. For silicon inspection, the stress optic coefficients in Eq. (2) will depend on this orientation as reported by Zheng and Danyluk in Eq. (1). However, utilizing this grey-field analysis, the directional dependence of the stress-optic coefficient of silicon does not complicate inspection as long as the stress-optic coefficients in two orthogonal orientations are known.

IV. CONSTRUCTION OF AN INFRARED GREY-FIELD POLARISCOPE

In the prototype IR-GFP a quartz tungsten halogen bulb was used as a near-infrared light source. This bulb was controlled through a dimmer switch to allow adjustable light intensity. A condensing lens was placed in front of the bulb to send as much light as possible through the polarizing optics and quarter wave plate. Figure 3 shows the optical setup, including the use of a frosted glass plate after the projecting optics to provide even illumination on the sample. Finally, to avoid thermal damage to the wire grids and polymer retardation plates, these optics were cooled using a squirrel cage fan. This source easily supplied enough power to obtain a strong signal through an as-lapped 0.8-mm-thick silicon wafer.

The detector unit utilized a visible light charge coupled device (CCD) camera with the stock glass IR filter replaced by a silicon filter to serve as an IR bandpass. A second polarizer was attached to a rotating mount with position detectors to determine the location of the polarizer axis during image acquisition. A 35 mm macro lens allowed a field of view ranging from approximately 3×4 mm to about 300 $\times 400$ mm depending on stand-off distance. This translates into an effective spatial resolution range of about 6 μm to 0.6 mm, respectively.

The advantages of this experimental configuration are important to enumerate. First, utilizing an off-the-shelf CCD camera provides a cost effective implementation of infrared
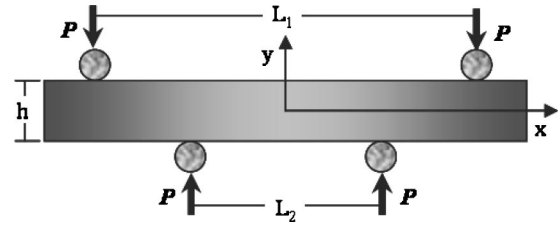
photoelasticity. Much of the expense of any full-field infrared system is involved in the military grade IR camera. Second, the current camera utilizes a 480×640 array detector, providing more than four times the number of pixels at the same magnification for typical 256×256 InGaAs near-IR cameras. Finally, this instrument can capture full-field residual stress images in approximately 10 s. This translates into inspection times of 10 s for a 100-mm-diam wafer at approximately 200 μm resolution, or less than 1 min for a spatial resolution of 100 μm. Thus, the grey-field implementation of infrared photoelasticity has potential for providing rapid, affordable, full-field residual stress characterization on the die level as well as the wafer level.

V. EXPERIMENTAL VALIDATION OF THE IR-GFP

Several experiments were conducted to verify the calibration of the instrument and compare experimental results to well-known theory. Two canonical geometries were explored; the four-point bend sample and the disk in compression. The four-point bend geometry provides a well-known stress distribution, while the disk in compression is commonly used to calibrate photoelastic materials and polariscopes. Both geometries are amenable to testing the brittle silicon substrate.

A. Four-point bend

A rectangular beam, measuring 44.5 mm long by 4.8 mm tall by 0.525 mm thick, was loaded in four-point bending, Fig. 4. The *x* and *y* axes lie along the vertical and horizontal directions with the origin in the center of the specimen. This load arrangement provides a constant bending moment between the inner span of the load points. The axial stress varies with distance from the neutral axis according to

$$\sigma_{xx} = -\frac{M_y}{I}, \tag{15}$$

where *M* is the applied moment and *I* is the beam moment of inertia. For portions of the beam away from the load points

$$\sigma_{yy} = 0. \tag{16}$$

Within the constant moment region, the transverse shear, *V*, is zero, such that there is no shear stress in the 0° orientation (τ_{xy}). For this specimen, all stress information will be captured in the $(\sigma_{xx} - \sigma_{yy})$ image

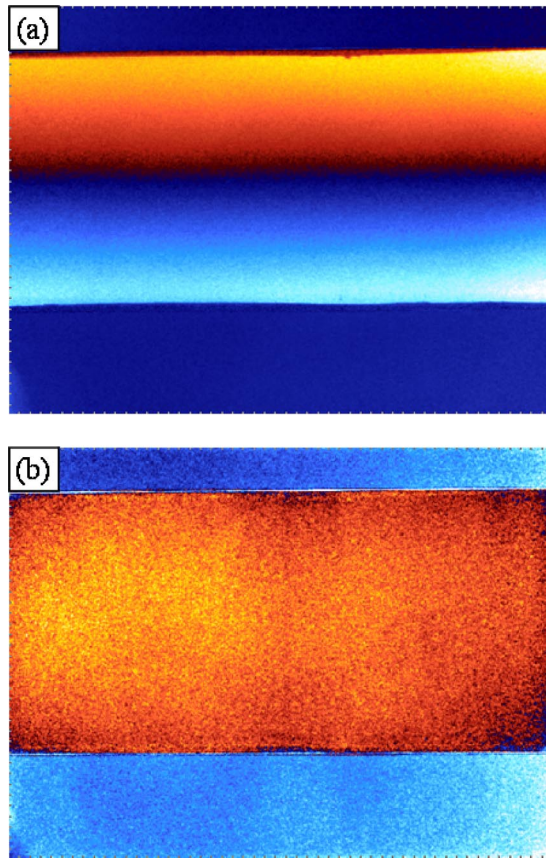$$\sigma_{xx} - \sigma_{yy} = -\frac{M_y}{I} \tag{17}$$

and for the given beam

FIG. 5. (Color online). IR-GFP images of a four-point bend specimen at an applied load of $P=3.9$ N (a) $(\sigma_x-\sigma_y)$, (b) $(\sigma_{+45}-\sigma_{-45})$.

$$M = \frac{1}{4}P(L_1 - L_2) \text{ and} \tag{18a}$$

$$I = \frac{1}{12}th^3, \tag{18b}$$

where P is the applied load, a is the moment arm, t and h are the specimen thickness and height, respectively. In these experiments, $L_1=31.8$ mm, $L_2=15.9$ mm, $t=0.525$ mm, and $h=4.8$ mm.

An Instron Mini 44 tabletop load frame was placed onto the optical work bench with the IR-GFP optics and used to apply load to the samples. The Mini 44 is a screw driven load frame operable in position control, with load measured using a 500 N load cell attached to the lower bending fixture. Small scale four-point bend fixtures are attached to the load frame as shown in Fig. 3. The silicon beam was cut from a 525-μm-thick, P-doped (100) double side polished wafer using a Disco Dicing saw and a Semitec S3045 diamond blade. The beams were cut along the [110] direction of the wafer with a misalignment of $\pm 1°$.

Typical infrared photoelastic data collected using the IR-GFP are shown in Fig. 5. The $(\sigma_{xx}-\sigma_{yy})$ image shows the expected stress distribution showing pure tension/compression in the x direction. Tensile stresses appear as shades of red above the neutral axis, while compressive stresses appear as shades of blue below the neutral axis. Grey-field theory easily distinguishes between tension and compression in this beam due to the opposite tilt of the el-
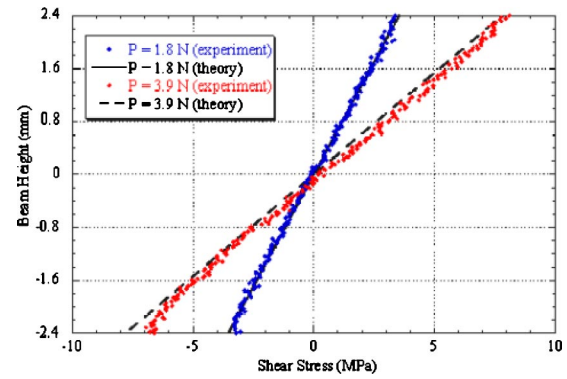

FIG. 6. (Color online). Comparison of theory and experimental results from the four-point bend experiments.

lipse associated with each direction. A traditional circular polariscope would not make this distinction because it only measures the ellipticity of the light, such that equal magnitudes of tension and compression are indistinguishable. As expected, the $(\sigma_{+45}-\sigma_{-45})$ image shows mostly noise resulting from no shear stress in this orientation for this test geometry.

Theoretical and experimental stress distributions, at applied loads of 1.8 and 3.9 N, are compared in Fig. 6. The experimental points represent pixel values from a line scan interrogation across the central portion of the beam, with no data smoothing or averaging across the length of the beam. Data are collected from the center of the constant moment section of the beam in order to eliminate any effect of the contact points. For this data set, all material property constants were obtained from the literature.[43] There is no need to calibrate the instrument to a specific material or fit data if the material properties are known ahead of time. Over most of the beam height, the experimental response is linear and compares quite well with theory. At the bottom section of the beam, the experimentally measured stress falls short of the maximum expected stress. This is most likely due to edge effects. Figure 6 shows that very low stresses can be resolved with this technique, even using a very thin silicon wafer. For both loading cases, the data are not obscured by noise and follow the expected linear trend with little scatter. A measure of stress resolution was calculated by measuring the deviation of adjacent data points about the expected linear trend. From these experiments the stress resolution was calculated to be 0.11 MPa. It is estimated that this resolution can be reduced by at least an order of magnitude by employing an optimized near-IR camera in the detection unit.

B. Disk in compression

A second validation experiment used a silicon disk in compression, Fig. 7. The judicious choice of the x axis aligned along the horizontal centerline of the disk results in a principal stress orientation. From linear isotropic theory of elasticity, the solutions for the normal stresses along the horizontal diameter are[48]

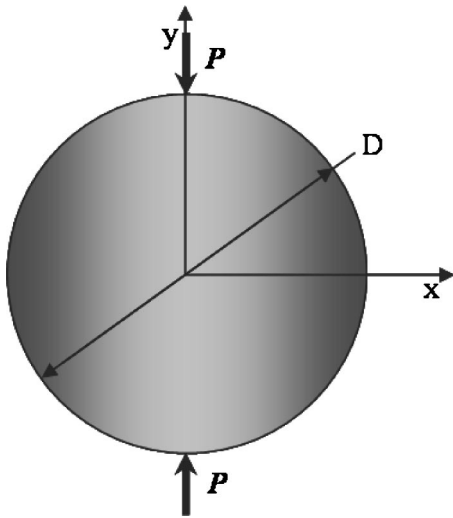$$\sigma_x = \sigma_1 = \frac{2P}{\pi h D}\left(\frac{D^2 - 4x^2}{D^2 + 4x^2}\right)^2, \tag{19}$$

FIG. 7. Disk in compression.

$$\sigma_y = \sigma_2 = -\frac{2P}{\pi h D}\left[\frac{4D^4}{(D^2 + 4x^2)^2} - 1\right], \tag{20}$$

where P is the applied load, h and D are sample thickness and diameter, respectively. The difference between these stresses is

$$\sigma_x - \sigma_y = \frac{8P}{\pi h D}\left[\frac{D^4 - 4D^2x^2}{(D^2 + 4x^2)^2}\right]. \tag{21}$$

At the centerline of the specimen, the $(\sigma_{+45} - \sigma_{-45})$ image will be null, but everywhere outside of this line this stress component has a nonzero value.

The experimental setup for the disk in compression is identical to that for the four-point bend experiments with the exception that compression platen fixtures are used to load the sample within the Instron Mini 44. These platens are polished and coated with a chrome finish, which reduces friction at the loading points. Masking tape is applied to the platens around the disk to reduce reflections from these platens (light reflected at a low angle will cause changes in polarization that confound the experiments). A 525-μm-thick, P-doped (100) double side polished silicon disk was diced to a 25 mm square using the Disco Dicing saw. Several hand grinding steps were then carried out to produce a disk using fixtures borrowed from optical lens making equipment. A final polish on the outer radial surface is carried out with a 1600 grit diamond wheel using water lubricant. The final disk diameter is 19.4 mm±0.25 mm. Despite efforts to produce smooth edges, some damage is encountered during specimen manufacture as well as handling and loading. As such, data near the sample edges are confounded by surface effects.

A representative IR-GFP image is shown in Fig. 8, at an applied load of 16.5 N. Figure 8(a) shows the symmetric portion of the shear stress while Fig. 8(b) image is antisymmetric about both the x and y axes as required by the symmetry of the specimen. These stress distributions match exactly with theory, and, again, show the sensitivity of the system. With a maximum stress in the center of the specimen of only 4 MPa, clean, noise-free images are acquired across
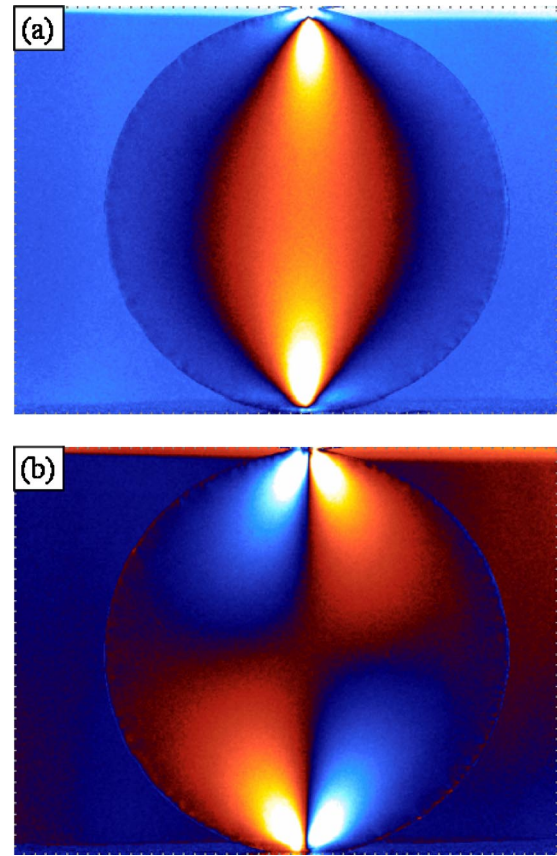

FIG. 8. (Color online). IR-GFP images of a silicon disk in compression at an applied load of $P = 16.5$ N. (a) $(\sigma_x - \sigma_y)$, (b) $(\sigma_{+45} - \sigma_{-45})$.

the entire specimen. Though a lower limit to the sensitivity was not sought, clean images were captured for applied loads as low as 0.95 N, which correspond to a *maximum* stress of 0.24 MPa along the horizontal diameter.

The disk-in-compression geometry is commonly used to determine the stress-optic coefficients of a material by counting the fringe order at the center of the specimen while increasing the applied load. As Fig. 8 shows, the stress levels investigated are decidedly subfringe. However, these results show that the stress-optic coefficients, as well as the sample orientation, can be obtained in a subfringe IR photoelastic experiment. A single crystal of silicon was loaded in a random orientation, as shown in Fig. 8. A line scan across the horizontal diameter of Fig. 8(a) is shown in Fig. 9. The stress distribution predicted by theory (solid line) is bounded by experimental data points gathered using the stress-optic coefficients assuming the sample was oriented in the [100] direction (lower curve) and the [110] directions (upper curve) in Fig. 9.

The actual stress-optic coefficient for the random orientation can be extracted by fitting the maximum experimental stress level to the theory for the given load using Eq. (1). The stress-optic coefficient for this sample orientation is approximately 1.46×10^{-11} Pa^{-1}, which is expected for an x-axis orientation of roughly 19° from the [110] direction. Using the fit coefficient, the functional form of the stress distribution nicely matches with theory except at the sample edges. This divergence is assumed to be due to the material damage
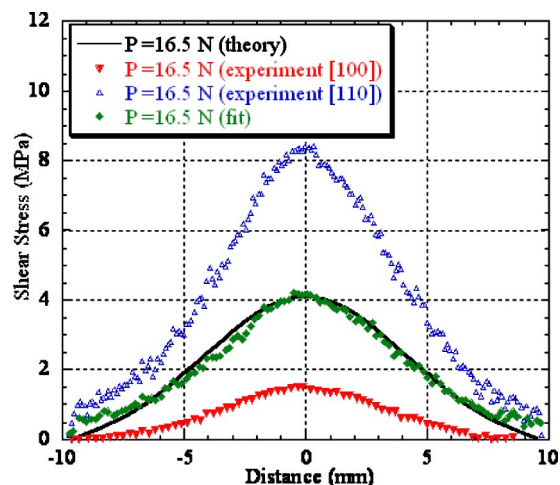
FIG. 9. (Color online). Stress distribution for a disk in compression. The open and filled triangles are experimental results with the min and max stress optic coefficient for silicon, while the green diamond represents the stress optic coefficient fit to theory.

encountered during specimen preparation and handling. For materials, or specific orientations of materials in which handbook values of the stress-optic coefficient are not available, the disk in compression geometry can be used as a subfringe calibration sample. This capability is especially useful for very thin semiconductor or other microelectronic materials that would require a load exceeding the ultimate strength to generate multiple fringes for traditional calibration.

VI. CURRENT AND FUTURE APPLICATIONS

The IR-GFP is being utilized in a growing list of laboratory and real-world applications, and many more initial investigations. The first utilization has been to inspect adhesively bonded semiconductor devices.[49] In this application, the IR-GFP has been shown to locate trapped particles that are undetectable using conventional infrared transmission (IRT) imaging. Figure 10 compares an IRT image (a) captured simultaneously with an IR-GFP image (b) where a single set of Newton's Rings in the middle of the IRT image identifies a defect, and a corresponding "bow-tie" pattern identifies the same defect in the IR-GFP image. This residual stress pattern in the IR-GFP image is expected from the indentation stress fields generated by trapped particles.[50] Along the right side of Fig. 10(b), a second smaller bow-tie pattern locates a defect that is too small to see with IRT imaging. For these particular samples, local variations in bond thickness generate optical interference patterns that obscure Newton's Rings in transmission imaging, yet have no effect on the ability of the IR-GFP to locate the residual stress signature. In a separate study, it has been shown that the IR-GFP can identify defects in fusion and anodically bonded silicon samples that cannot be discerned with IRT imaging.[51] As the IR-GFP allows measurement of the stress state associated with each of these trapped particles, it is possible to quantify the effects of these defects on the residual stress budget of components built from bonded substrates.

Furthermore, the trapped particles that generate large residual stresses in the silicon substrates are easily differenti-
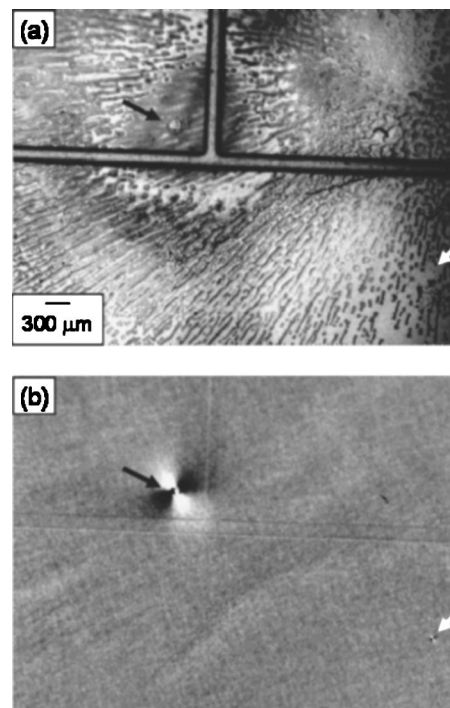

FIG. 10. Adhesively bonded microfluidic device with trapped particles. (a) IRT image; (b) shear stress image from IR-GFP.

ated from gas bubbles confined to reside in the adhesive layer, defects which do not result in significant residual stresses. Infrared transmission imaging detects defects either through contrast effects or the presence of Newton's Rings while the IR-GFP detects defects by measuring their stress fields. The advantage of the IR-GFP is seen by contrasting Figs. 10 and 11, where Newton's Rings due to trapped par-
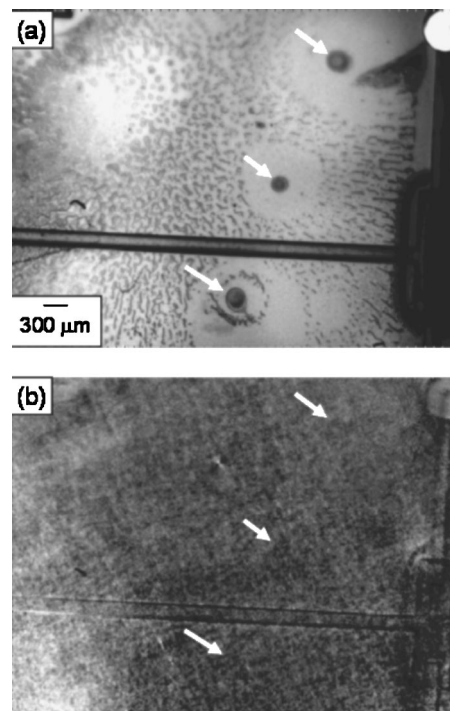

FIG. 11. Adhesively bonded microfluidic device with trapped gas bubbles. (a) IRT image; (b) shear stress image from IR-GFP.
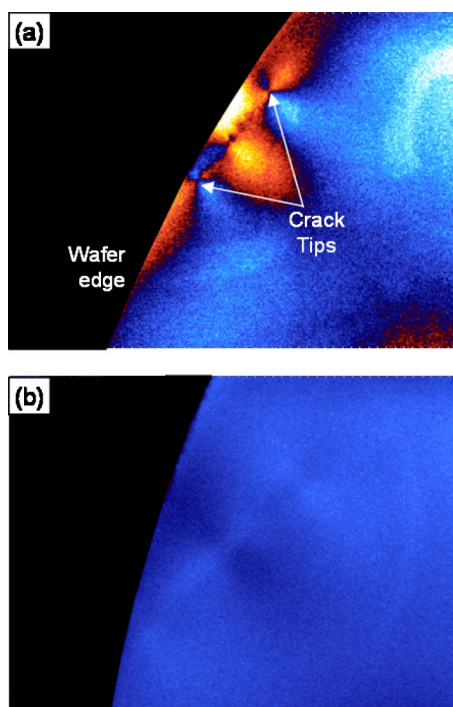
FIG. 12. (Color online). IR-GFP images of an as-lapped silicon wafer that show (a) cracking, and (b) no damage along the wafer edge.

ticles in Fig. 10(a) are identical to those generated by bubbles in Fig. 11(a), while the IR-GFP shows clear differences in the stress magnitudes of each defect type.

The IR-GFP has also been utilized to inspect silicon wafers early in the wafering process to locate cracking prior to further processing.[52] Despite the very rough wafer surfaces from dicing, surface cracking is easily, and rapidly, located. Figure 12(a) shows an IR-GFP image of a portion of the wafer with a shallow surface crack that did not propagate through the 0.8 mm wafer thickness. Figure 12(b) shows a defect free region of the same wafer. The residual stress pattern surrounding the cracked region allows rapid identification of damaged substrates early in the wafering process. The rough surface finish of these wafers would make reliable inspection with a single-point laser source difficult. With the current IR-GFP prototype, a full 300 mm wafer can be inspected in less than 5 min at 100 μm spatial resolution. In another study, the IR-GFP was used to quantify the residual stress profile across these silicon wafers, which can be related to process control parameters.

Current projects utilizing the IR-GFP include: further defect quantification in anodic and fusion bonded structures, residual stress measurements arising from bonding patterned wafers, inspection of silicon photovoltaic sheets, and inspection of infrared windows used in both military and commercial industries. In these applications, the IR-GFP has shown the ability to be used as a quality and process control tool as well as for research and development.

[1] T. Vreeland, A. Dommann, C.-J. Tsai, and M.-A. Nicolet, Mater. Res. Soc. Symp. Proc. **130**, 3 (1989).
[2] S. K. Wang, C. C. Lee, and C. S. Tsai, Proceedings of the IEEE Ultrasonics Symposium, Phoenix, AZ, p. 171 (October 26–28, 1977).
[3] A. K. Sinha, H. J. Levinstein, and T. E. Smith, J. Appl. Phys. **49**, 2423 (1978).
[4] P. A. Flinn, D. S. Gardner, and W. D. Nix, IEEE Trans. Electron Devices **34**, 689 (1987).
[5] G. G. Stoney, Proc. R. Soc. London, Ser. A **82**, 172 (1909).
[6] J. A. Floro, E. Chason, and S. R. Lee, Mater. Res. Soc. Symp. Proc. **406**, 491 (1996).
[7] E. Chason, J. Yin, K. Tetz, R. Beresford, L. B. Freund, M. Gonzalez, and J. A. Floro, Mater. Res. Soc. Symp. Proc. **583**, 167 (2000).
[8] D. Post, B. Han, and P. Ifju, *High Sensitivity Moiré: Experimental Analysis for Mechanics and Materials* (Springer, New York, 1995).
[9] H. Nuerge and J. Schwider, Optik (Stuttgart) **111**, 319 (2000).
[10] M. Jozwik, A. Sabac, and C. Gorecki, Proc. SPIE **4655**, 760 (2002).
[11] H. V. Tippur, S. Krishnaswamy, and A. J. Rosakis, Int. J. Fract. **52**, 91 (1991).
[12] A. J. Rosakis, R. P. Singh, Y. Tsuji, E. Kolawa, and N. R. Moore, Jr., Thin Solid Films **325**, 42 (1998).
[13] D. Brewster, Philos. Trans. R. Soc. London **106**, 156 (1816).
[14] E. G. Coker and L. G. N. Filon, *A Treatise on Photoelasticity* (Cambridge University Press, Cambridge, 1931).
[15] W. C. Dash, Phys. Rev. **98**, 1536 (1955).
[16] A. V. Appel and D. A. Pontarelli, J. Opt. Soc. Am. **48**, 289 (1958).
[17] S. R. Lederhandler, J. Appl. Phys. **30**, 1631 (1959).
[18] G. L. Cloud and J. T. Pindera, Exp. Mech. **8**, 193 (1968).
[19] R. O. DeNicola and R. N. Tauber, J. Appl. Phys. **42**, 4262 (1971).
[20] S. Redner, Strain **15**, 58 (1979).
[21] R. W. Dixon, J. Appl. Phys. **38**, 5149 (1967).
[22] C. W. Higginbotham, M. Cardona, and F. H. Pollak, Phys. Rev. **184**, 821 (1969).
[23] H. Kotake, K. Hirahara, and M. Watanabe, J. Electrochem. Soc. **127**, 179 (1980).
[24] M. Yamada, Appl. Phys. Lett. **47**, 365 (1985).
[25] M. Yamada, Rev. Sci. Instrum. **64**, 1815 (1993).
[26] M. Yamada, M. Fukuzawa, N. Kimura, K. Kaminaka, and M. Yokogawa, Seventh Conference on Semi-insulating Materials, 1992, p. 201, Ixtapa, Mexico (April 21–24, 1992).
[27] T. Kawase, T. Wakamiya, S. Fujiwara, K. Hashio, K. Kimura, M. Tatsumi, T. Shirakawa, K. Tada, and M. Yamada, in Ref. 26, p. 85.
[28] M. Yamada, J. Appl. Phys. **74**, 2463 (1993).
[29] M. Yamada, J. Appl. Phys. **74**, 6435 (1993).
[30] M. Herms, M. Fukuzawa, M. Yamada, J. Klober, G. Zychowitz, and J. R. Niklas, Mater. Sci. Eng., B **66**, 7 (1999).
[31] M. Hermsm, M. Fukuzawa, V. G. Melov, J. Schreiber, P. Mock, and M. Yamada, J. Cryst. Growth **210**, 172 (2000).
[32] M. Fukuzawa and M. Yamada, J. Electron. Mater. **25**, 337 (1996).
[33] M. Yamada, K. Ito, and M. Fukuzawa, International Conference on Indium Phosphide and Related Materials, 1997, p. 209, Cape Cod, MD, (May 11–15, 1997).
[34] M. Fukuzawa, M. Herms, M. Uchida, O. Oda, and M. Yamada, International Conference on Indium Phosphide and Related Materials, 1998, p. 537, Tsukuba, Japan (May 11–15, 1998).
[35] M. Fukuzawa and M. Yamada, J. Cryst. Growth **229**, 22 (2001).
[36] Y. Niitsu, K. Ichinose, and K. Ikegami, AMD (Am. Soc. Mech. Eng.) **187**, 29 (1994).
[37] Y. Niitsu and K. Gomi, AMD (Am. Soc. Mech. Eng.) **187**, 37 (1994).
[38] Y. Niitsu and K. Gomi, Adv. Electron. Packag. **26**, 833 (1999).
[39] H. Liang, Y. Pan, S. Zhao, G. Qin, and K. Chin, J. Appl. Phys. **71**, 2863 (1992).
[40] S. P. Wong, W. Y. Cheung, N. Ke, M. R. Sajan, W. S. Guo, L. Huang, and S. Zhao, Mater. Chem. Phys. **51**, 157 (1997).
[41] S. P. Wong, H. J. Peng, and S. Zhao, Appl. Phys. Lett. **79**, 1628 (2001).
[42] T. Zheng and S. Danyluk, Proceedings of the Society of Experimental Mechanics Annual Conference, 2001, p. 658, Portland, OR (June 4–6, 2001).
[43] T. Zheng and S. Danyluk, J. Mater. Res. **17**, 36 (2002).
[44] H. D. Geiler, W. Kurner, and O. Storbeck, Mater. Res. Soc. Symp. Proc. **591**, 249 (2000).
[45] H. D. Geiler, M. Wagner, H. Karge, M. Paulsen, and R. Schmolke, Mater. Sci. Semicond. Process. **5**, 445 (2002).
[46] J. R. Lesniak, STTR Final Report (Contract No. NAS1-97036, 2000).

[47] J. R. Lesniak, M. J. Zickel, C. S. Welch, and D. F. Johnson, Proceedings of the Society of Experimental Mechanics Annual Conference, 1997, p. 219, Bellevue, WA (June 2–4, 1997).

[48] J. W. Dally and W. F. Riley, *Experimental Stress Analysis* (McGraw–Hill, New York, 1991).

[49] G. Horn, T. Mackin, J. Lesniak, and B. Boyce, Exp. Tech. **28**, 19 (2004).

[50] G. Horn, Ph.D. dissertation, University of Illinois at Urbana-Champaign (July 2004).

[51] G. Horn, T. Mackin, and J. Lesniak, Exp. Mech. (submitted).

[52] A. Richards, J. Lesniak, and G. Horn, Photonics Spectra **38**, 34 (2004).